European Journal of Mechanics / A Solids 113 (2025) 105689

Contents lists available at ScienceDirect

European Journal of Mechanics / A Solids

journal homepage: www.elsevier.com/locate/ejmsol

Full length article

Practical methods for the implementation of material strength into an Eulerian hydrocode

M.D. Fitzgerald [a,b,*], D.E. Eakins [a], N. Petrinic [a], E. Leggett [a], N. Niasse [b], J.D. Pecover [b]

[a] Department of Engineering Science, University of Oxford, Parks Rd, United Kingdom
[b] First Light Fusion Ltd., Oxford Industrial Park 10, Meads Rd, United Kingdom

ARTICLE INFO

MSC:
00-01
99-00

Keywords:
Material strength
Johnson Cook
Impact
Eulerian
Hydrocode

ABSTRACT

This study presents the framework and implementation of a material strength model within a two-step Eulerian solution scheme in the MHD hydrocode, B2. The techniques presented in this work provide practical solutions to problems encountered when modelling high strain-rate behaviour of solids in an Eulerian framework. Several novel methods developed in this work resulted in the accurate reproduction of a Taylor anvil-on-rod test in B2 without a complex and computationally expensive interface reconstruction technique. These methods include a complete algorithmic definition of the different components of the stress tensor, ensuring realistic behaviour in low-density mixed cells at the rod-vacuum boundary through a density dependent modification of the yield, implementing automatically generated slip conditions at part boundaries, and damping oscillating numerical instabilities induced by the inclusion of strength. The Taylor test served as a rigorous verification case for the strength model, demonstrating the efficacy of these novel methods. A cross-code comparison against the results of a Lagrangian simulation in Ansys AUTODYN, a well-benchmarked commercial code which employs Young's Reconstruction, of the Taylor rod deformation revealed a close match with the rod profile predicted by B2. In this article, emphasis is placed on the practical details of the routines required to implement these corrections to facilitate the adoption of three-dimensional material strength models in other Eulerian hydrocodes.

1. Introduction

Hydrocodes simulate physical phenomena through the evaluation and evolution of forces and displacements at select points within a discretised space. The manner in which the materials and space are defined can vary, with two common approaches being the Lagrangian and Eulerian formulations. In the Lagrangian formulation, materials are represented by a grid of points that move with the material flow, while in the Eulerian formulation, materials are defined within a fixed domain through which they can move. The accuracy of either formulation strongly depends on the physical processes being modelled. Systems characterised by rapid deformation, such as those featuring shock or fluid flow, are typically better represented using an Eulerian grid; Lagrangian meshes become entangled when representing systems with considerable deformation and require high computational resource in three-dimensions due to the large strains typically encountered during these processes. Conversely, systems with highly-resolved interfaces, such as solid components and damage processes (such as crack propagation), are more accurately captured in Lagrangian space. These limitations of the differing discretisation methods introduce difficulties when attempting to model systems that experience both rapid deformation and material strength effects, such as the implosion of liners for inertial confinement fusion (Pecover and Chittenden, 2015) and electromagnetic flyer acceleration (Lemke et al., 2003; Fitzgerald et al., 2025). Given that mesh entanglement and computational expense preclude the use of Lagrangian formulations in these scenarios, researchers instead use Eulerian or Arbitrary Lagrangian–Eulerian (ALE) hydrocodes with material strength models.

Incorporating a material strength model into an Eulerian hydrocode appears conceptually simple. The calculations of strain rate, stress and the subsequent addition of the behaviour of strength to the forces and work done can be accomplished using differencing schemes and established constitutive models. However, accurately capturing the dynamic behaviour of materials in real-world scenarios within an Eulerian framework poses notable challenges. Material strength effects are easier to conceptualise using a Lagrangian framework, where forces between atoms (discrete points) organised into larger structures resist deformation. In an Eulerian scheme, strain rates are calculated between cells in the mesh in each direction, leading to components of the stress tensor in different locations in the cell, which require manipulation to derive momentum and energy contributions in a single cell-based

---

* Corresponding author at: Department of Engineering Science, University of Oxford, Parks Rd, United Kingdom.
E-mail address: mila.fitzgerald@physics.ox.ac.uk (M.D. Fitzgerald).

https://doi.org/10.1016/j.euromechsol.2025.105689
Received 11 September 2024; Received in revised form 2 April 2025; Accepted 23 April 2025

location (McGlaun et al., 1990). Additionally, in an Eulerian grid, the default interaction between adjacent material surfaces assumes perfect bonding, unlike the Lagrangian framework where surfaces in contact possess independent velocity fields. Where a Lagrangian scheme requires a defined contact algorithm to prevent material interpenetration, an Eulerian scheme employs a single continuous velocity grid across the entire mesh, ensuring the conservation of mass, momentum, and energy while preventing non-physical material mixing. This unified velocity field effectively bonds all cells together, leading to the unphysical generation of shear stress between separate solid material components (Anderson, 1987). Typically, contact algorithms and reconstruction of the material interface are introduced to ensure accurate behaviour at material-material and material-vacuum interfaces.

Investigations aimed at enhancing the accuracy of the simulation of solids in Eulerian hydrocodes have been relatively limited. Benson et al. compared Eulerian and ALE methods of implementing slip conditions to model a Taylor anvil-on-rod test, including the behaviour at the rod-anvil and rod-vacuum interface (Benson and Okazawa, 2004). The Eulerian formulation utilised mixture theory to adjust the stress tensor such that the shear stress was zero on the contact plane (Walker and Anderson Jr., 1994). However, Benson ultimately found mixture theory to be inadequate for modelling the Taylor rod-anvil interaction, instead representing the anvil as a rigid body with independent velocity fields (Benson, 1997, 1992). More commonly, interface reconstruction methods, such as Young's Reconstruction (Youngs, 1982), can be employed to capture solid deformation more accurately. However, these techniques are computationally expensive and complex to implement, restricting the ability to model material strength to highly specialised Eulerian hydrocodes. To circumvent this issue, researchers often resort to non-physical workarounds, such as manually predefining interfaces between parts. Burkett et al. conducted studies on dynamic tensile extrusion tests using the two-dimensional Eulerian code, MESA. In these experiments, copper and tantalum projectiles were accelerated in a gas gun to velocities ranging between 330 and 700 m/s and extruded through a high-strength steel die (Burkett, 2019). The interaction between the projectile and the die was achieved by defining a layer of cells along the inner surface of the die, within which the components of the stress tensor was set to zero. This enabled the projectile to pass through the computational mesh at the projectile-die interface with minimal artificial drag induced by the hydrocode's vertex-centred velocity scheme. Although effective, the requirement to manually define interfaces hinders repeatability between simulations and becomes challenging to implement in systems with many different moving parts.

In this work, the implementation of a material strength model in B2, an in-house Eulerian hydrocode developed by FLF, is presented. B2 operates using a two-step Eulerian solution scheme across a fixed rectangular mesh, the details of which can be found in McGlaun et al. (1990). Material strength effects were integrated into the first (Lagrangian) step, where the force and work done in each cell are computed. The second (Eulerian) step maps the distorted cells back to the mesh using a second-order MUSCL advection scheme. In this article, the fundamental equations for material strength are derived mathematically. Then, the novel aspects of the strength algorithm are presented, including:

- The structure of the differencing scheme to calculate stress, force, and work done in each cell.
- A density dependence factor incorporated into the calculation of the yield value.
- The implementation of automatically generated slip conditions.
- The introduction of an artificial viscosity term to damp numerical instabilities instigated by extreme shear gradients.

These aspects were developed to allow the hydrocode to accurately predict solid deformations within simulations without reconstructing or predefining the interfaces, which is a complex and computationally costly procedure. The efficacy of these solutions in the strength model then evaluated through verification against Taylor anvil-on-rod tests generated in the commercially available code, Ansys AUTODYN (Autodyn, 2005). As noted by Benson et al. the Taylor rod-anvil interaction is a rigorous test-case; complex behaviour within the rod, at the rod-anvil, and at the rod-vacuum interfaces must be captured to accurately predict the overall rod deformation. The results of this cross code comparison with Ansys AUTODYN were then used to evaluate the efficacy of the novel methods introduced in this work.

2. Mathematical model of the material strength algorithm

In this section, necessary details of the material strength algorithm implemented in B2 are presented, including the derivation of the force and work terms that are calculated in the mesh, details of the constitutive model, and information about interface tracking methods.

2.0.1. Governing equations

When simulating a solid using an Eulerian hydrocode, the fundamental equations contain no assumptions about the material state. Instead, this information is accounted for within the equation of state and transport coefficients. The standard MHD equations assume the pressure tensor is isotropic. Thus, to represent shear forces, the anisotropic pressure terms in the momentum and energy equations must be reinstated, which may be written as,

$$\rho\frac{\partial v}{\partial t} + v\cdot\nabla v = -\nabla \boldsymbol{P} + \boldsymbol{J}\times\boldsymbol{B} + \nabla\cdot\underline{\underline{s}}, \tag{1a}$$

$$\frac{\partial U}{\partial t} + v\cdot\nabla U = -P\nabla\cdot v - \nabla\cdot q + \boldsymbol{J}\cdot\underline{\underline{\eta}}\cdot\boldsymbol{J} + \underline{\underline{s}} : \nabla v, \tag{1b}$$

where ρ is the density, v is the velocity, $\boldsymbol{P}$ is the pressure, $\boldsymbol{J}$ is the current density, $\boldsymbol{B}$ is the magnetic field strength, U is the internal energy, q is the charge, $\underline{\underline{s}}$ is the stress tensor and $\underline{\underline{\eta}}$ is the resistivity.

The stress tensor is calculated from the strain ($\underline{\underline{\epsilon}}$), and can be expressed using Einstein's summation notation as:

$$s_{ij} = 2\eta_k(\epsilon_{ij} - \delta_{ij}\epsilon_{ii}), \tag{2}$$

where η_k is the kinematic viscosity and δ_{ij} is the Kronecker delta function. The terms in the strain rate tensor ($\underline{\underline{\dot{\epsilon}}}$) are given by,

$$\dot{\epsilon}_{ij} = \frac{1}{2}\left(\frac{\partial v_i}{\partial x_j} + \frac{\partial v_j}{\partial x_i}\right), \tag{3}$$

where x is the spatial coordinate. The strain rate tensor can be divided into a 'hydrostatic' part, which describes the change in volume without distortion, and a 'deviatoric' part, which describes distortion without a change in volume. The hydrostatic component of the strain rate tensor is already accounted for in the pressure scalar, thus only the deviatoric strain rate and stress tensor need be included.

In a solid, stresses are accumulated over time, hence the relationship between stress and strain may be represented in the Lagrangian form as,

$$\frac{\partial s_{ij}}{\partial t} = 2G(\dot{\epsilon}_{ij} - \delta_{ij}\dot{\epsilon}_{ii}), \tag{4}$$

where G is the shear modulus and $\dot{\epsilon}_{ii}$ cancels the hydrostatic component already accounted for. In Cartesian coordinates, this term becomes,

$$\dot{\epsilon}_{ii} = \frac{1}{3}\left(\frac{\partial v_x}{\partial x} + \frac{\partial v_y}{\partial y} + \frac{\partial v_z}{\partial z}\right). \tag{5}$$

The shear modulus implemented in B2 is density and temperature (T) dependent, such that,

$$G(\rho, T) = 3K(\rho, T)\frac{1-2v}{2(1+v)}, \tag{6}$$

where K is the bulk modulus and v is the material specific Poisson Ratio. The bulk modulus as a function of density and temperature can be derived from the equation of state,

$$K(\rho, T) = \rho\frac{\partial P(\rho, T)}{\partial \rho} = \rho c^2(\rho, T), \tag{7}$$

where c is the adiabatic sound speed. The shear wave velocity (c_s),

$$c_s = \sqrt{\frac{G}{\rho}}, \tag{8}$$

is incorporated into the total material sound speed.

2.0.2. Yield model

When a force is applied to a solid, it will deform elastically (returns to its original shape) if the stress developed is below the yield stress (Y) of the material. When this is the case, the relationship between stress and dimensionless strain is linear. However, if the stress is considered larger than the yield stress, the material will deform plastically (the deformation is permanent). Beyond the yield stress, the relationship between stress and strain ceases to be linear and the material accumulates plastic strain (ε_p). When modelling this process, it is convenient to calculate the trial stress tensor (s^*_{ij}) using Eq. (4), and subsequently reduce the stress based on Y, which can be calculated using a constitutive model. In this work, if the von Mises effective stress ($\sigma^*_{\rm eff}$) of the trial stress tensor,

$$\sigma^*_{\rm eff} = \sqrt{\frac{3}{2} s^*_{ij} s^*_{ij}}, \tag{9}$$

is less than the yield stress (Y), the material is considered to be elastic and the trial stress deviator is accepted (Westerling, 2002). However, if the opposite is found to be true, the new stress deviator (s_{ij}) is calculated as,

$$s_{ij} = \frac{Y}{\sigma^*_{\rm eff}} s^*_{ij}. \tag{10}$$

This is essentially a uniformly scaled-down version of the trial stress deviator. The plastic strain rate $\dot{\varepsilon}_p$ accumulated on exceeding yield can then be calculated using,

$$\Delta\dot{\varepsilon}_p = \frac{\sigma^*_{\rm eff} - Y}{3G dt}, \tag{11}$$

where dt is the explicit timestep. This contributes to ε_p through,

$$\varepsilon_p = \varepsilon_p + \Delta\dot{\varepsilon}_p dt. \tag{12}$$

To capture both the linear elastic and plastic deformation behaviour of a material, its yield stress was calculated at each cell-centre using the Johnson–Cook (**JC**) model, such that,

$$Y = (A + B\varepsilon_{\rm p}p^n)(1 + C ln(\varepsilon^*_{\rm p}))(1 - (T/T_{\rm melt})^m), \tag{13}$$

where A, B, and C are material specific coefficients, m is the softening exponent, n is an exponent, $\varepsilon_{\rm p}$ is the plastic strain and $\varepsilon^*_{\rm p}$ is the dimensionless plastic strain rate, and $\varepsilon^*_p = \dot{\varepsilon}_p/\dot{\varepsilon}_{p0}$ with $\dot{\varepsilon}_{p0} = 1\ {\rm s}^{-1}$ (Johnson and Cook, 1985).

2.0.3. Force and work terms

Once the stress tensor has been determined, the force and work done on the material can be calculated. The additional force, given by $\nabla \cdot \underline{\underline{s}}$, is analogous to the force created at a pressure gradient. In Cartesian geometry, the components of the force vector are given by,

$$F_x = \frac{\partial s_{xx}}{\partial x} + \frac{\partial s_{xy}}{\partial y} + \frac{\partial s_{xz}}{\partial z}, \tag{14a}$$

$$F_y = \frac{\partial s_{xy}}{\partial x} + \frac{\partial s_{yy}}{\partial y} + \frac{\partial s_{yz}}{\partial z}, \tag{14b}$$

$$F_z = \frac{\partial s_{xz}}{\partial x} + \frac{\partial s_{yz}}{\partial y} + \frac{\partial s_{zz}}{\partial z}. \tag{14c}$$

The work done due to the stress tensor, given by $\underline{\underline{s}} : \nabla v$, is analogous to the $P\nabla \cdot v$ work term. It can be expanded in Cartesian coordinates to give,

$$\begin{aligned}\underline{\underline{s}} : \nabla v = {} & s_{xx}\frac{\partial v_x}{\partial x} + s_{xy}\frac{\partial v_x}{\partial y} + s_{xz}\frac{\partial v_x}{\partial z} + s_{xy}\frac{\partial v_y}{\partial x} + s_{yy}\frac{\partial v_y}{\partial y} + s_{yz}\frac{\partial v_y}{\partial z} \\ & + s_{xz}\frac{\partial v_z}{\partial x} + s_{yz}\frac{\partial v_z}{\partial y} + s_{zz}\frac{\partial v_z}{\partial z}.\end{aligned} \tag{15}$$

2.0.4. Interface tracking methods

Interface-tracking methods are indispensable in Eulerian systems to mitigate numerical diffusion across the material boundaries, a crucial consideration when monitoring the movement of solid materials. The precise location of the part boundaries plays a pivotal role in defining their contact behaviour. In B2, the conserved values at the material interfaces are tracked using the volume of fluid (VoF) method, the details of which can be found in Benson (2002). Briefly, this involves representing the fluid interface using a colour function, which tracks the fraction of a material within a given cell. This colour function is used to modify total cell variables, such as the overall density or sound speed of the cell. The VoF method has been shown to effectively model fluid systems with large deformations and is relatively simple to implement. This interface tracking technique can be followed by a reconstruction of the material interface in each cell based on the colour function. One of the most accurate methods of reconstructing interfaces in a system involving solid materials is Young's Reconstruction (Youngs, 1982). This method involves the definition of the interface shape as a linear surface segment inside partially filled cells, improving sharpness and accuracy of the solution compared to the VoF method without reconstruction. However, Young's Reconstruction is both complex to implement and can require significant additional computational cost for normal estimation and interface reconstruction. Consequently, instead of implementing a surface reconstruction in B2, a number of novel solutions were employed within our strength model algorithm that allow it to predict the deformation of solids with sufficient accuracy. These solutions are designed to be simple to encode and have low computational cost, facilitating their adoption in other Eulerian hydrocodes.

3. Novel aspects of the strength algorithm

In this section, the novel features implemented in our strength algorithm are presented. These features permit the modelling of complex solid deformation in an Eulerian hydrocode without an expensive interface reconstruction, and slip conditions without the manual definition of separate parts within a simulation. For clarity going forward, the logical variable locations in the mesh are defined in Fig. 1. Each variable is referenced in terms of the x coordinate index (i), y coordinate index (j), and z coordinate index (k). B2 derives conserved variables at the cell-centre, thus, in this work (i, j, k) refers to the cell-centred location. All cell-centred quantities are assumed to be uniform across the cell. The face-centred velocities, denoted for ease by an underscored 'f', are perpendicular to the cell face they are located on. In this work, the notation is simplified by thinking of the face-centred velocities as existing in a staggered mesh. For example, the velocity in the x-direction (v_{fx}) can be written as

$$v_{fx}(i, j, k) = v_x(i - \frac{1}{2}, j, k). \tag{16}$$

It is important to note the face-centred velocities are derived independently from the cell-centred velocities at the beginning of the Lagrangian step. Two-dimensional and one-dimensional meshes referenced in this section are sub-cases of the three dimensional mesh. All quantities discussed were temporally positioned at the start of the timestep.

3.0.1. Face-centred stress formulation

The contributions of the strength model to the total momentum and internal energy in each timestep requires the differential of the velocity across the mesh to be taken to calculate the stress, followed by the further differential of this stress to find the force and work terms. However, there are no examples in available in open literature of how these stresses, force, and work terms should be calculated. In this work, it was found that using cell-centred velocities to calculate face-centred stresses, which are then compared to the yield and accumulated

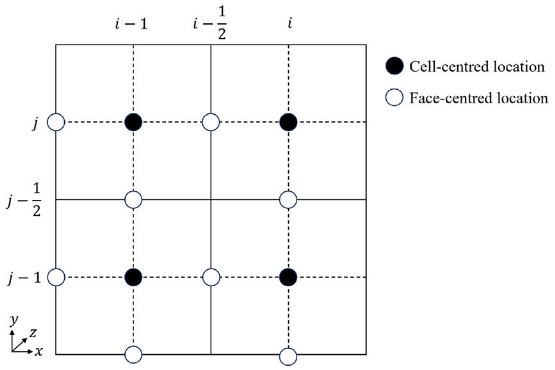

Fig. 1. The original and staggered Eulerian mesh with the cell-centred and face-centred locations marked.

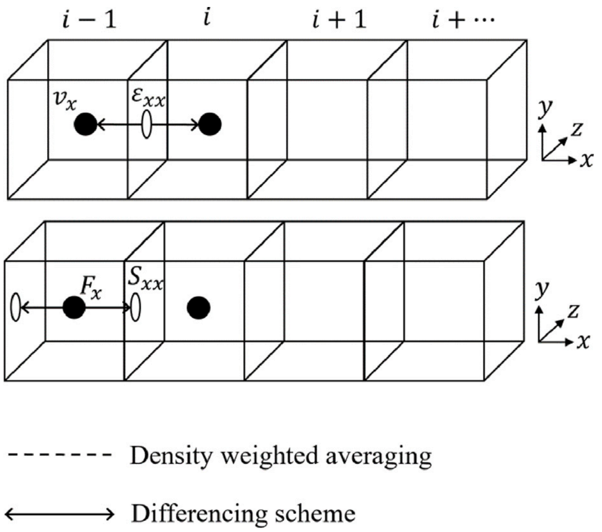

Fig. 2. Illustration of Face-Centred Stress algorithm in one-dimension, which was ordered in such a way to result in a cell-centred force and work value.

in place, produced the most successful results. In this face-centred stress algorithm, a forward spatial differencing scheme was used to calculate face-centred components of the strain rate tensor for each timestep. The force and work terms were then calculated at the cell-centre using a backward spatial differencing scheme. In this scheme, Eq. (3) for a diagonal component of the strain rate tensor (for instance, $\dot{\varepsilon}_{xx}$) becomes,

$$\dot{\varepsilon}_{xx} = \frac{\partial v_x}{\partial x} = \frac{v_x(i-1) - v_x(i)}{dx}, \tag{17a}$$

where v_x is the cell-centred velocity in the x-direction and dx is the distance between the cell-centres. Variables in an Eulerian mesh must be in the same location in order to be summed. Consequently, non-diagonal components of the strain rate tensor were calculated such that the gradient of the velocities involved in the summation have answers in the same location. For example, the equation for the shear strain rate component $\dot{\varepsilon}_{yx}$ becomes,

$$\begin{aligned}\dot{\varepsilon}_{yx} &= \frac{1}{2}\left(\frac{\partial v_x}{\partial y} + \frac{\partial v_y}{\partial x}\right)\\ &= \frac{1}{2}\left(\frac{v_{fx}(i,j+1) - v_{fx}(i,j-1)}{2\cdot dy} + \frac{v_y(i-1,j) - v_y(i,j)}{dx}\right),\end{aligned} \tag{18a}$$

and results in $\dot{\varepsilon}_{yx}$ being located at x-face. This equation is visualised in Fig. 3(a).

Referring to the locations of the hydrostatic component of the strain rate tensor $\dot{\varepsilon}_{ii}$ in Eq. (5), it can be observed that $\frac{\partial v_x}{\partial x}$, $\frac{\partial v_y}{\partial y}$, and $\frac{\partial v_z}{\partial z}$ cannot be added directly, as they exist on different faces. To account for this, three face-centred components of $\dot{\varepsilon}_{ii}$ were calculated at each face. For example, at the x-face Eq. (5) in two-dimensions $(x-y)$ becomes,

$$\begin{aligned}\dot{\varepsilon}_{ii}(i-\frac{1}{2},j,k) = \frac{1}{3}\Bigg[&\frac{v_x(i-1,j,k) - v_x(i,j,k)}{dx}\\ &+ 0.25\left(\frac{(v_y(i-1,j-1,k) - v_y(i-1,j+1,k)) + (v_y(i,j-1,k) - v_y(i,j+1,k))}{dy}\right)\Bigg].\end{aligned} \tag{19}$$

The location of the nine components of the stress tensor on three different faces of the cell also complicates the calculation of the yield behaviour of the system. Referring to Eq. (9), it becomes clear σ^*_{eff} cannot be calculated unless all the components of the trial stress tensor are in the same cell location. Hence, following the calculation of the trial stress tensor, a single cell-centred component of σ^*_{eff} was found using,

$$\sigma^*_{\text{eff}}(i,j,k) = \sqrt{\frac{3}{2}\underline{\underline{s^*}}(i,j,k)\underline{\underline{s^*}}(i,j,k)}, \tag{20}$$

where $\underline{\underline{s^*}}$ is the cell-centred trial stress tensor. If the mesh size is constant, then $\underline{\underline{s^*}}(i,j,k)$ can be found for each cell using,

$$\begin{aligned}\underline{\underline{s^*}}(i,j,k) = \frac{1}{2}\Big(&(s_{xx}(i-\frac{1}{2},j,k) + s_{xx}(i+\frac{1}{2},j,k)) + (s_{yx}(i-\frac{1}{2},j,k)\\ &+ s_{yx}(i+\frac{1}{2},j,k)) + (s_{zx}(i-\frac{1}{2},j,k) + s_{zx}(i+\frac{1}{2},j,k))\\ &+ (s_{xy}(i,j-\frac{1}{2},k) + s_{xy}(i,j+\frac{1}{2},k)) + (s_{yy}(i,j-\frac{1}{2},k)\\ &+ s_{yy}(i,j+\frac{1}{2},k)) + (s_{zy}(i,j-\frac{1}{2},k) + s_{zy}(i,j+\frac{1}{2},k))\\ &+ (s_{xz}(i,j,k-\frac{1}{2}) + s_{xz}(i,j,k+\frac{1}{2})) + (s_{yz}(i,j,k-\frac{1}{2})\\ &+ s_{yz}(i,j,k+\frac{1}{2})) + (s_{zz}(i,j,k-\frac{1}{2}) + s_{zz}(i,j,k+\frac{1}{2}))\Big).\end{aligned} \tag{21}$$

The yield stress was then calculated using the constitutive equation at the cell-centre. This permitted the direct calculation of a single cell-centred plastic strain, using,

$$\varepsilon_p(i,j,k) = \frac{\sigma^*_{\text{eff}}(i,j,k) - Y(i,j,k)}{3G(i,j,k)}. \tag{22}$$

However, as shown in Fig. 2, this formulation requires the face-centred stresses to be reduced in place, such that the resulting force vector and work done are cell-centred. To achieve this, the yield at each cell face (Y_f) was calculated using a density-weighted average. For example, the face-centred yield at the lower x-face of the cell was found using,

$$Y_{fx}(i,j,k) = Y(i-\frac{1}{2},j,k) = \frac{Y(i,j,k)\rho(i-1,j,k) + Y(i-1,j,k)\rho(i,j,k)}{\rho(i-1,j,k) + \rho(i,j,k)}. \tag{23}$$

The face-centred value of the von Mises effective stress was then found using the density-weighted average of $\sigma^*_{\text{eff}}(i-1,j,k)$ and $\sigma^*_{\text{eff}}(i,j,k)$. The components of the trial stress tensor were then reduced using the corresponding face-centred values of the yield and von Mises effective stress.

Upon determining the accepted stress tensor, the contributions to the cell-centred force vector and work done due to material strength were calculated. The force in the x-direction (F_x) is calculated using Eq. (14b). However, the locations of the components of stress (S_{ij}), displayed in Fig. 3(b), demonstrate the gradient of S_{yx} cannot be calculated in the y-direction in its native position on the x-face of the cell. Instead, S_{yx} must first be calculated at the y-face using simple averaging. In two-dimensions $(x-y)$, F_x becomes,

$$F_x(i,j) = \frac{(S_xx(i-\frac{1}{2},j) - S_xx(i+\frac{1}{2},j))}{dx} + \frac{(S_{xy}(i,j-\frac{1}{2}) - S_{xy}(i,j+\frac{1}{2}))}{dy}$$

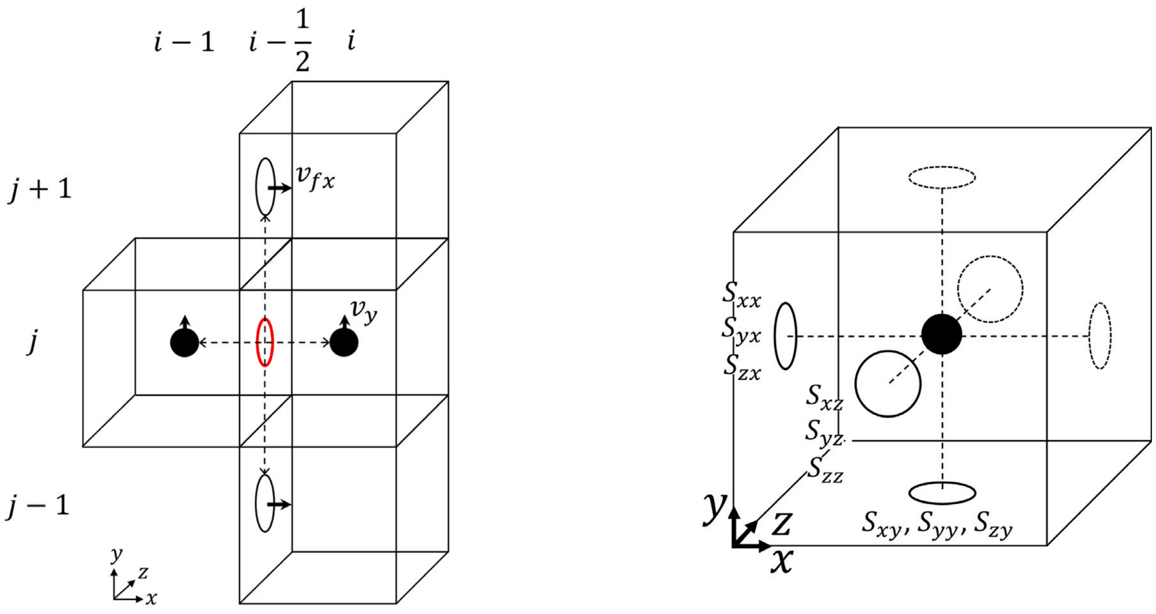

(a) An illustration of the calculation of $\dot{\varepsilon_{yx}}$ (Equation 18).

(b) Locations of the nine components of the stress tensor on the three cell faces.

Fig. 3. The method for calculating the shear strain rate $\dot{\varepsilon_{yx}}$ alongside the final location of the nine components of the stress tensor.

$$+0.25\left[\frac{(S_{yx}(i-\frac{1}{2},j)+S_{yx}(i+\frac{1}{2},j))-(S_{yx}(i-\frac{1}{2},j-1)+S_{yx}(i+\frac{1}{2},j-1))}{dx}\right]. \tag{24}$$

Calculating the work done also requires the components of the accepted stress tensor be recalculated at the cell-centre. For example, in two dimensions $(x-y)$, Eq. (15) becomes,

$$\begin{aligned} W_{strength}(i,j) = 0.5 \Bigg[& (S_{xx}(i-\frac{1}{2},j)+S_{xx}(i+\frac{1}{2},j))\left(\frac{v_{fx}(i,j)-v_{fx}(i+1,j)}{dx}\right) \\ & +(S_{yx}(i-\frac{1}{2},j)+S_{yx}(i+\frac{1}{2},j))\left(\frac{v_{fx}(i,j)-v_{fx}(i+1,j)}{dx}\right) \\ & +(S_{xy}(i,j-\frac{1}{2})+S_{xy}(i,j+\frac{1}{2}))\left(\frac{v_{fy}(i,j)-v_{fy}(i,j+1)}{dx}\right) \\ & +(S_{yy}(i,j-\frac{1}{2})+S_{yy}(i,j+\frac{1}{2}))\left(\frac{v_{fy}(i,j)-v_{fy}(i,j+1)}{dx}\right)\Bigg]. \end{aligned} \tag{25}$$

3.1. Yield density dependence factor

In an Eulerian framework, accurately representing the strength of a material near interfaces is challenging due to the inherent dependence on grid resolution. Without an interface reconstruction method, partially filled cells at the material boundary can lead to artificially high yield stress, affecting the accuracy of deformation predictions. Eq. (13) demonstrates that the cell-centred yield calculated using the Johnson Cook model has no reliance on the cell density. While this is appropriate in a Lagrangian framework, where each point has a known mass, it can cause unphysically high yield in partially filled Eulerian cells. Without using an interface reconstruction method, the definition of a solid part's interface in an Eulerian mesh is only as detailed as the grid resolution. As illustrated in Fig. 4, a cell filled with a certain volume fraction of some solid material with density (ρ_s) is interpreted in Eulerian space as a cell with a total density proportional to the volume fraction multiplied by ρ_s. As the yield is not density dependent, a cell with a low volume of solid material, such as cell a in Fig. 4, will erroneously have the same yield as a fully filled cell. This can lead to inaccuracy in the material deformation at the boundary of the solid part adjacent to vacuum. To correct this, the yield was artificially adjusted in low density cells using the density factor (Φ) proposed by Pecover (2015), whereby,

$$Y_{modified} = \Phi \cdot Y, \tag{26a}$$

$$\Phi = \begin{cases} e^{\frac{-(\rho - f\rho_s)^2}{\Delta}}, & \text{if } \rho < f\rho_s, \\ 1.0, & \text{if } \rho \geq f\rho_s. \end{cases} \tag{26b}$$

In this equation, f is the density fraction below which the yield should be reduced, Δ is a scaling constant set to 1000 m^6/kg^2 (Pecover and Chittenden, 2015), and Φ is the factor by which the yield is reduced. The exponential form of this equation was chosen by Pecover et al. to ensure the yield stress was unaffected above $f\rho_s$, yet decreased rapidly and smoothly to zero below $f\rho_s$. However, Pecover et al. used a value $f = 1.0$, which was not found to be an effective choice. In this work, f was found to be a parameter capable of improving the accuracy of the Taylor rod impact simulation. The impact of varying f is shown in Fig. 5; if $\rho \geq f\rho_s$, the occupation of material in the cell is high enough that the yield should be unmodified, thus Φ is set to 1.0. However, if the material density in the cell drops below this threshold, the exponential ensure the yield is rapidly and smoothly reduced to zero, indicating the loss of material strength. The tuning of this equation to find an appropriate value for f is discussed in Section 5.1.1.

3.2. Implementation of slip conditions

Enforcing slip conditions (frictionless contact) in Eulerian simulations is particularly challenging for complex geometries, where manual definition of interfaces can be computationally expensive and impractical. While existing methods modify the yield condition at the interface, they often require predefined regions or separate material definitions, limiting their applicability to dynamic and intricate simulations. To address this, an automated approach for imposing frictionless contact at both material-material and material-vacuum boundaries is presented in this section.

The stress formulation developed in this work, as discussed in Section 3.0.1, calculates three stresses at each cell face. This is done by taking the gradient of the velocity between cell centres using a forward spatial difference scheme. To prevent the calculation of stress between two separate parts, it is common to modify the entire stress tensor in the

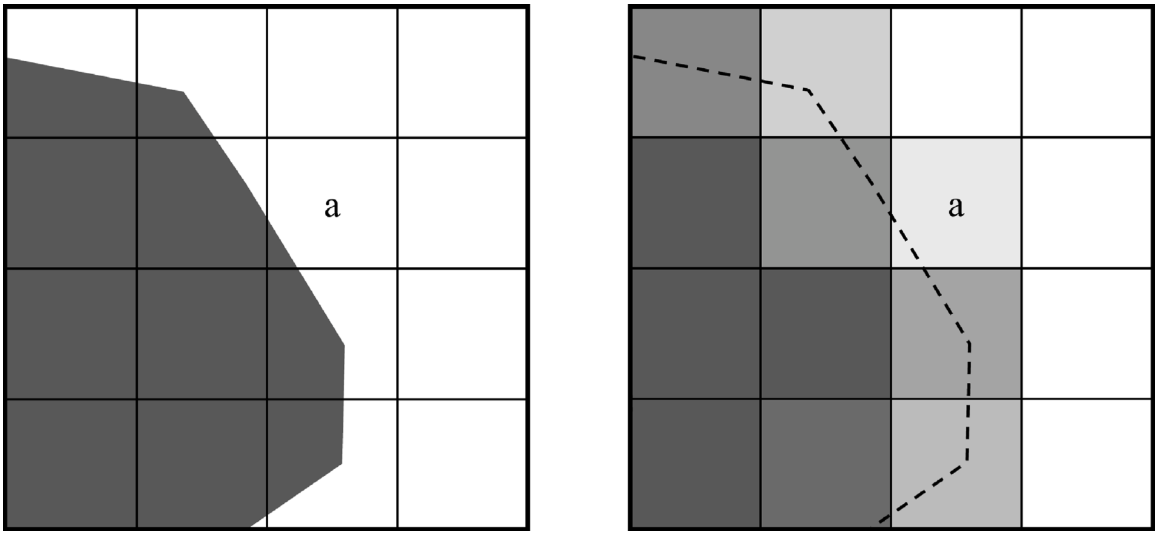

Fig. 4. Illustration showing the representation of a solid shape in an Eulerian grid. In the uncorrected JC model, cell a will have the same yield as a fully occupied cell.

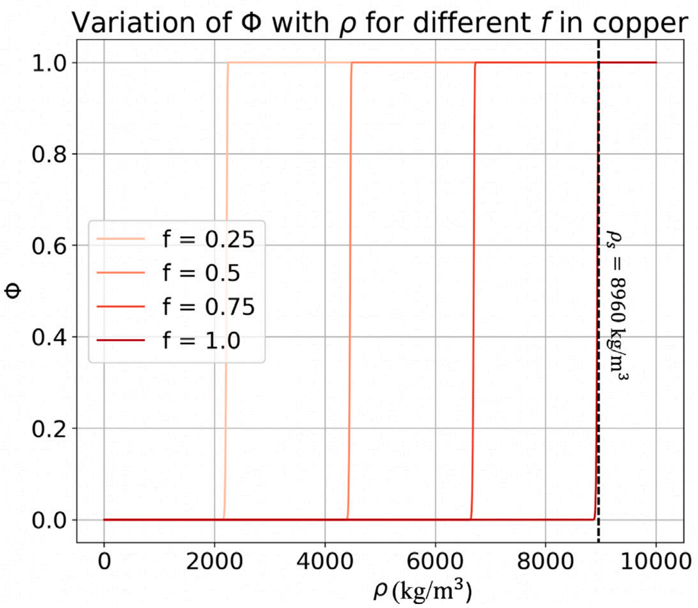

Fig. 5. Δ for different values of f in copper, where $\rho_s = 8960$ kg/m^3. If $\rho < f\rho_s$, the yield in the cell is rapidly and smoothly reduced to zero i.e. the material in the cell is no longer included in material strength calculations as its density is too low.

cell at the material boundary to be zero (Benson and Okazawa, 2004). However, in this work, only the components of the strain rate at the cell face at the boundary between separate parts were set to zero to represent a frictionless boundary. This boundary is identified in a cell in place by querying the material number in the cells surrounding it and whether these materials have a yield of greater than zero. For example, in the x-direction, if a cell at (i, j, k) and the cell behind it at $(i-1, j, k)$ both have a yield of greater than zero and the same material number, a value of 1 was assigned in this position. If either cell has a different material number, or yield of zero, a 0 was assigned in this position in the grid instead. When repeated in each direction, this creates three face-centred arrays made up of 1s and 0s, referred to in this work as the interface grid (IG). An illustration of this process is shown in Fig. 6. The IG was used to implement slip conditions at material-material and material-vacuum interfaces by directly modifying the strain rate calculation, such that Eq. (17) became

$$\dot{\varepsilon}_{yy}(i, j-\frac{1}{2}, k) = \frac{v_x(i, j-1, k) - v_x(i, j, k)}{dx} \cdot IG_y(i, j, k). \tag{27a}$$

By multiplying the face-centred stress components with the value of the interface grid calculated at that face, an artificial slip condition is introduced. For example, in the cell labelled b in Fig. 6, $IG_y(i, j, z) = 0.0$, thus $\dot{\varepsilon}_{yy} = 0.0$, enforcing slip conditions between the separate material parts.

The interface grid also prevents non-physical shear strain rates being calculated the material-vacuum interface. Fig. 3(a) demonstrates the S_{yx} in cell (i, j, k) is calculated by taking the gradient of the velocity between $v_y(i, j, k)$ and $v_y(i-1, j, k)$, and $v_{fx}(i, j-1, k)$ and $v_{fx}(i, j+1, k)$. This ensures S_{yx} is a face-centred value which exists at $(i-1/2, j, k)$. However, the gradient between $v_{fx}(i, j-1, k)$ and $v_{fx}(i, j+1, k)$, and $v_y(i, j, k)$ and $v_y(i-1, j, k)$, can introduce extreme shear forces at the rod-vacuum interface. To avoid this, Eq. (18) was modified to become

$$\dot{\varepsilon_{yx}} = \left(\frac{1}{2}\left(\frac{v_y(i-1, j, z) - v_y(i, j, z)}{dx} + \frac{v_{fx}(i, j+1, z) - v_{fx}(i, j-1, z)}{2 \cdot dy} \times IG_x(i, j+1, z) \cdot IG_x(i, j-1, z)\right)\right) \cdot IG_x(i, j, z). \tag{28}$$

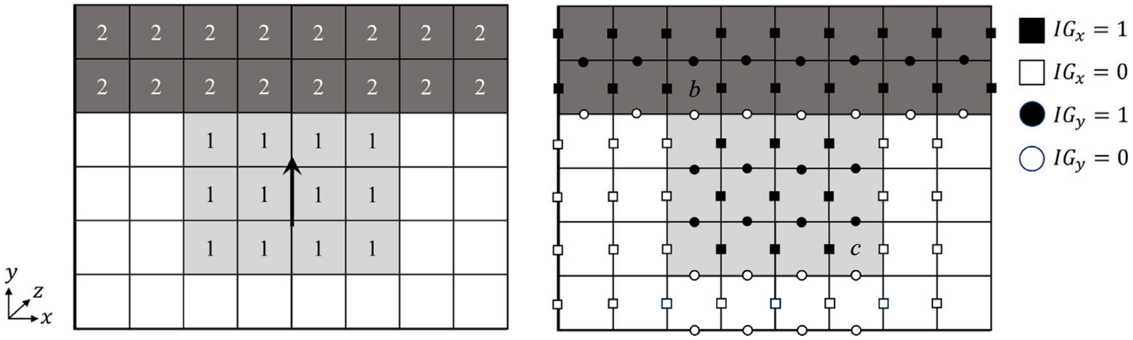

Fig. 6. Depiction of the interface grid in two-dimensions in a domain with Material 1 and Material 2. The interface grid is set to 1 at the x face of cell (i, j, k) if $(i-1, j, k)$ if both have the same material number and $Y > 0$. Cells labelled b and c are used to illustrate the effect of the interface grid in Eqs. (27) and (28).

This scenario can be illustrated by calculating $\dot{\varepsilon}_{yx}$ for the cell labelled c in Fig. 6 using Eq. (28). Here, $v_{fx}(i, j-1, z) = 0.0$ as it is a vacuum cell, and if material 1 has some velocity $v_{fx}(i, j+1, z) > 0.0$. Around cell c, $IG_x(i, j, z) = IG_x(i, j+1, z) = 1.0$ but $IG_x(i, j-1, z) = 0.0$, thus $\dot{\varepsilon}_{yx}$ reduces to $\frac{1}{2}\frac{v_y(i-1,j,z) - v_y(i,j,z)}{dx}$. This ensures physical shear between the filled cells is still captured, while excluding the extreme gradient that would exist between the material and vacuum cells from the calculation.

Overall, the interface grid provides an efficient mechanism for enforcing material boundaries by modifying flux values, preventing the unphysical advection of stress and plastic strain. By computing the IG once per dimension, the method significantly reduces computational overhead, replacing costly conditional checks with simple multiplicative operations. Furthermore, as the IG is constructed locally using only nearest-neighbour cell states, it remains fully compatible with grid-based parallelisation, ensuring scalability for complex simulations.

3.3. Shear wave instabilities

In an Eulerian hydrocode without a constitutive model, changes in momentum and internal energy occur only in the direction of fluid motion. However, when a strength model is introduced, shear stresses generate momentum and internal energy changes in directions orthogonal to the flow. In B2, this led to the propagation of significant numerical instabilities in shear-dominated regions for both stress formulations described in the previous section. These instabilities can be demonstrated using a simple 1D finite element solver, as illustrated in Fig. 7, which depicts a simplified domain designed to highlight instability propagation due to shear forces. In this setup, copper-filled cells aligned along the x-direction experience a velocity gradient in the y-direction, activating only the S_{yx} stress component. If the system is allowed to evolve without modification, the velocity in cells adjacent to the gradient interface exhibits numerical instabilities that propagate along with the shear waves. This behaviour is shown in Fig. 8, where the velocity on either side of the original interface develops oscillations with amplitudes of approximately 5 m/s, corresponding to 10% of the system's initial velocity.

While the occurrence of numerical instabilities at steep velocity gradients is a familiar concept, it is typically encountered at the jump discontinuities associated with shock waves. These are dealt with by the introduction of pressure-like viscosity terms, designed to smear the shock front over three to four cells (VonNeumann and Richtmyer, 1950). In this work, a similar approach was applied to the issue of numerical ringing in regions dominated by shear force was found to successfully dampen the instabilities. By drawing a parallel to Christensen's approximate Riemann solver (Benson, 1992), the shear wave artificial viscosity term (q) was calculated using the following equation,

$$q = \Delta v_{ij}\left(\frac{\rho Z^{-} + \rho^{-} Z}{\rho^{-} + \rho}\right) \tag{29a}$$

$$Z = \sqrt{\rho G}, \tag{29b}$$

where Δv_{ij} refers to the difference between the cell centred velocities v_i in the direction j, Z is the shear wave impedance and the — notation refers to the cell centred value to the left of the current cell being considered. This smoothly and effectively dissipates the numerical ringing created at the shear velocity gradient, as demonstrated in Fig. 8(b). By extending the concept of artificial viscosity to shear-dominated regions, this approach successfully mitigates numerical ringing at velocity gradients, providing a robust and computationally efficient solution for stabilising strength models in Eulerian hydrocodes.

4. Test case: Taylor anvil-on-rod

The strength model in B2 was verified using a cross-code comparison with Lagrangian simulations performed in Ansys AUTODYN-2D (AUTODYN) (Autodyn, 2005). AUTODYN is an explicit dynamics simulation program for solving short-duration, severe-loading problems. The code has been used extensively to model scenarios such as the Taylor anvil-on-rod test (Volkov et al., 2017; Eakins and Thadhani, 2006), thus its solution to the test case provides a suitable benchmark by which the accuracy of the strength model integrated into B2 can be evaluated. The Taylor anvil-on-rod test, introduced by Taylor in 1948 (Taylor, 1948), is a widely used method for characterising dynamic material deformation at strain-rates up to 10^4 s^{-1}. In this test, a high-velocity rod impacts an anvil, resulting in high strain rates at the impact face, which gradually decrease along the length of the rod. Fig. 9 illustrates a typical test configuration, highlighting the key regions of interest analysed in this work. Upon impact, the rod undergoes significant plastic deformation, flaring outward at the impact face and exhibiting 'barrelling' further down its length. Historically, the final rod length was used to estimate the material's dynamic yield stress; however, subsequent studies revealed that tracking the rod's evolving profile provides deeper insights into localised plastic flow and stress distributions (Eakins and Thadhani, 2006). The Taylor test serves as a rigorous validation case for material strength models, as the rod's deformation profile is highly sensitive to the material's stress response, yield behaviour, and plastic flow.

For this study, the impact was approximated using a plate-on-plate configuration, where two identical copper plates, moving with equal and opposite velocities, collided in vacuum, as shown in Fig. 10. The two-dimensional planar simulations were performed with a 0.1 mm mesh resolution in both codes. Although some test cases used a rigid anvil, the plate-on-plate configuration was primarily analysed for the cross-code comparison. To prevent numerical welding, the two plates were treated as separate parts in B2, despite both being modelled as copper. B2 employed the Frankfurt Equation of State (**FEOS**) (Faik et al., 2018) for the copper rod, a semi-analytical, tabulated equation of state based on the QEOS model (Kemp and Meyer-ter Vehn, 1998). To ensure a close comparison, the AUTODYN simulations were configured

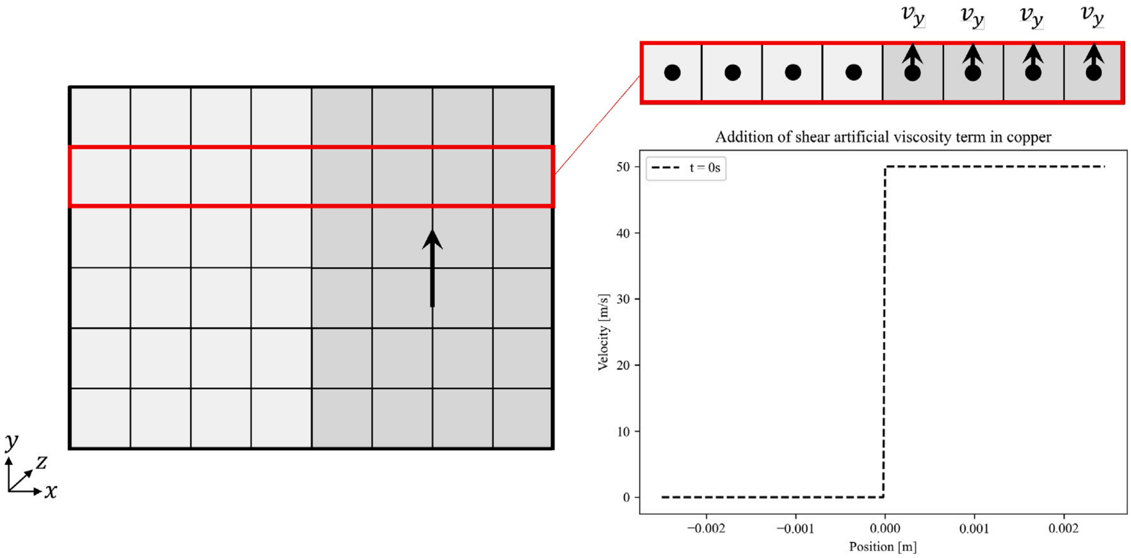

Fig. 7. Diagram of the 1D system used to investigate shear forces.

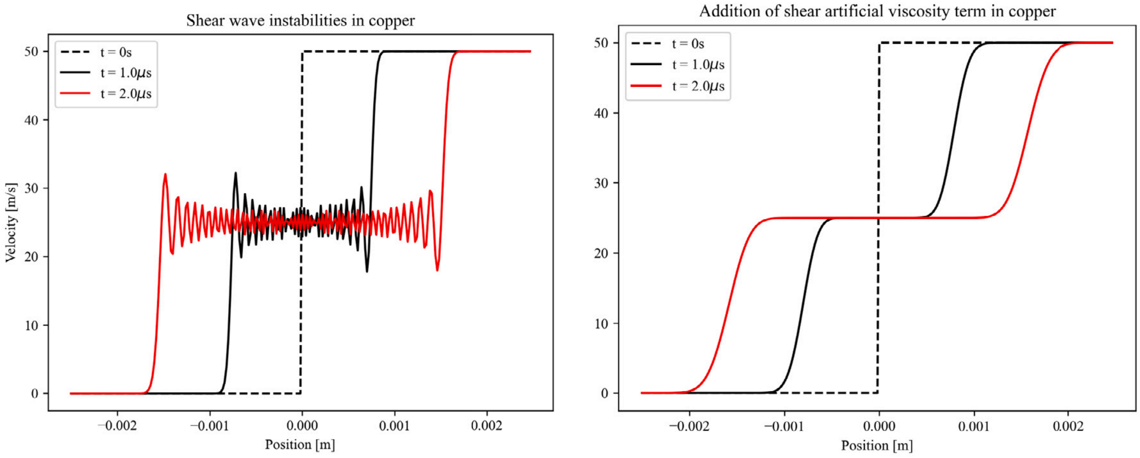

(a)

(b)

Fig. 8. Results from the 1D solver showing plots with and without the shear wave artificial viscosity modification. The simulation without artificial viscosity in B2 begins to develop complex structures, which are not present in the AUTODYN simulation.

Table 1
Johnson–Cook material properties.

Material	A	B	C	n	m	Melting temp
Copper	90 MPa	292 MPa	0.025	0.31	1.09	1356 K

with a linear equation of state, where ρ = 8.96 g/cc, K = 129 GPa, G = 46 GPa and the specific heat capacity c_h = 3.84×$^{-4}$ kJ/gK. The difference in equations of state is expected to have a negligible effect on rod deformation, as FEOS closely approximates the linear EOS at low temperatures. Both B2 and AUTODYN used the same Johnson–Cook (**JC**) (Johnson and Cook, 1985) material parameters for copper, listed in Table 1. Additionally, frictionless contact conditions were enforced at the interface in both codes to maintain consistency. It is important to note that AUTODYN employs Young's Reconstruction, which was discussed in Section 2.0.4.

5. Results

The comparison between the Taylor anvil-on-rod test case in B2 and AUTODYN provides a stringent validation of the strength model, demonstrating that the Eulerian implementation in B2 accurately reproduces the expected plastic deformation behaviour observed in well-established Lagrangian simulations. First, the effectiveness of the methods introduced in this study were assessed. Then, a more thorough analysis of results of the cross code comparison between B2 and AUTODYN is presented.

5.1. *Impact of novel methods*

In this section, the efficacy of the novel methods described in Section 3 are demonstrated using the Taylor anvil-on-rod test case.

5.1.1. *Tuning of the yield density dependence factor*

The choice of the density fraction parameter, f, plays a critical role in ensuring accurate deformation behaviour at the rod-vacuum interface, balancing numerical stability and physically realistic results. If f is set too low, the algorithm calculates strain rates between low-density mixed cells at the rod-vacuum interface and the main body of the rod, resulting in shear forces accelerating the low density cells to unphysically high velocities. This process is depicted in Fig. 11, where f = 0.1 in the copper rod. Extreme velocities in low density cells at

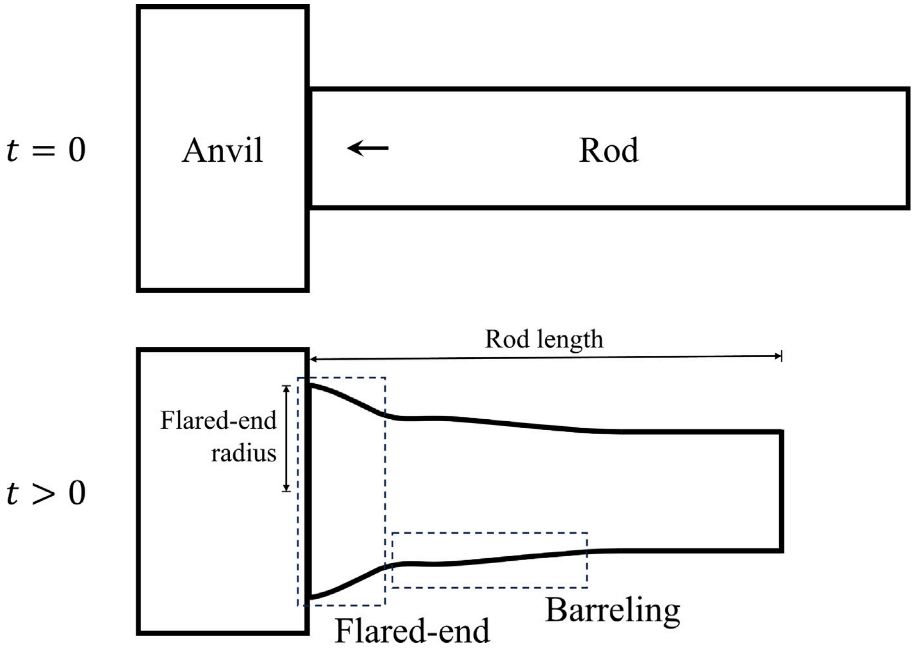

Fig. 9. Depiction of Taylor anvil-on-rod test, including terminology used throughout this work.

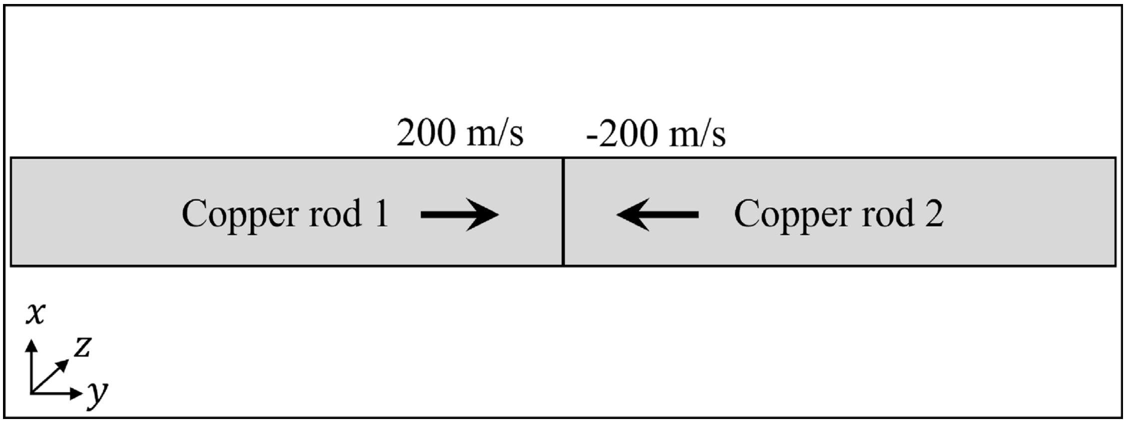

Fig. 10. Simulation set-up of the Taylor anvil-on-rod test in B2 and AUTODYN, approximating the rigid anvil by performing a symmetric plate impact.

the interface led to severe reduction in the explicit Eulerian timestep, resulting in excessively high simulation runtimes. By contrast, if f was too high the interface became prone to unrealistic deformation in material with density below the cut-off. Fig. 12 depicts the difference between a rod with $f = 0.4$ and $f = 0.5$: Fig. 12(a) demonstrates a clear loss of accuracy in the solution at the rod-vacuum interface profile.

Ultimately, it was determined that the Taylor anvil-on-rod simulation performed well with a value of $f = 0.4$. It is proposed that this value of f is not specific to the rod material in this scenario, but instead an inherent feature of the form of the density dependence factor. When the density in the cell is below $0.4\rho_s$, which can otherwise be thought of as when the cell is a little under half full, the yield is smoothly and rapidly reduced to zero. For material at solid density, this is the equivalent of only calculating strain rates between cells at the material-vacuum interface that are over half full. As a result, it is highly likely this form of the density dependence will be valid other materials.

5.1.2. Impact of the interface grid at rod-anvil boundary

In the Taylor test, the interface grid ensured velocity gradients were only taken between cells within the Taylor rod itself. Without this modification, material at rod-vacuum interface deformed, blurring the interface and reducing the accuracy of the solution. Figs. 13(a)–13(b) show an example of this behaviour in the Taylor rod in B2. The instabilities formed at the rod-vacuum interface were particularly prominent along the length of the rod, away from the flared-end. Similar instabilities were observed in the Eulerian version of the Taylor rod simulation in AUTODYN. Thus, the proposed grid modification proves to be a more accurate approach for simulating the interface dynamics in this scenario than Young's Reconstruction (see Fig. 14).

5.1.3. Shear wave instabilities in Taylor rod

The Taylor rod deformation testcase simulated in B2 was sensitive to the effect of the shear wave instabilities. The cumulative effects of the numerical ringing introduced by the unsuppressed instabilities in the rod are shown in the images from simulations shown in Fig. 15. As the simulation progresses, the rod begins to develop complex structures, which are not present in the AUTODYN simulation, at the flared-end. The result at 50 μs with the shear wave artificial viscosity term and without is plotted in Fig. 16. The figure demonstrates this term significantly improves the match between the rod profile in B2 and

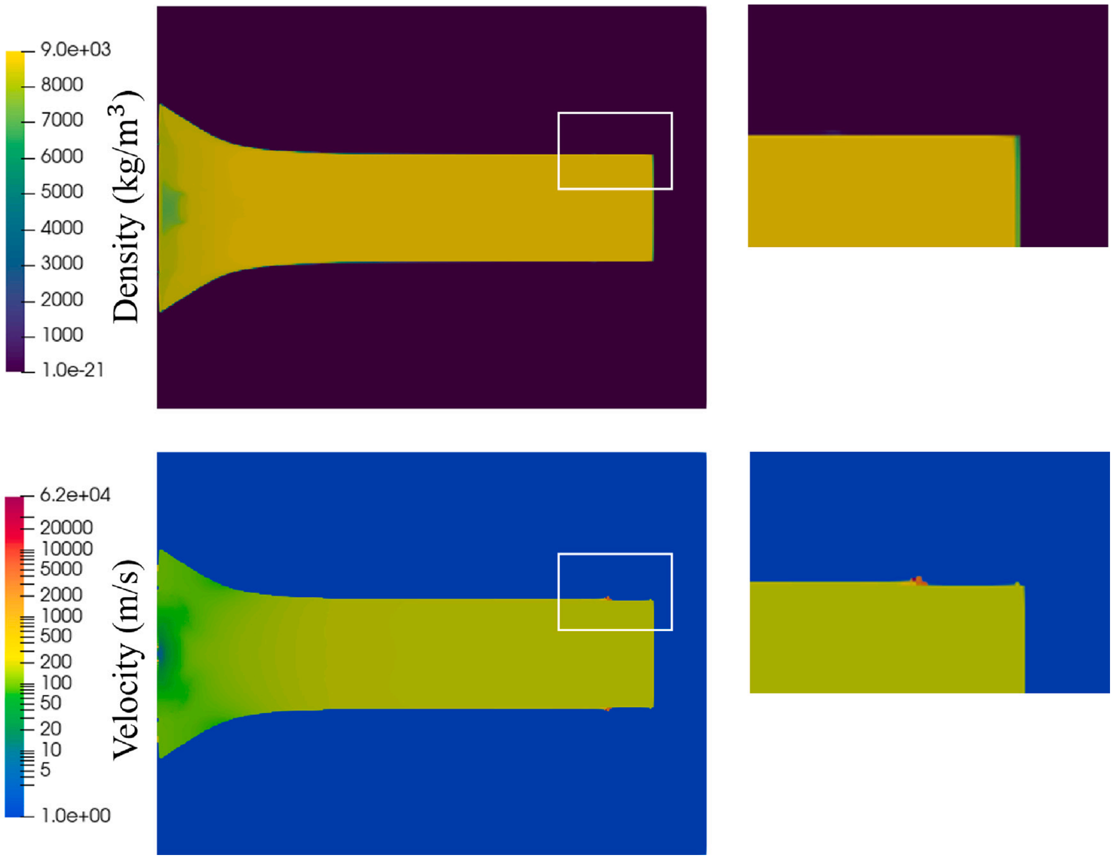

Fig. 11. A frame in B2 from a simulation without a density-factor corrected yield. The frames highlight high-velocity low-density material at the rear of the rod, which result in excessively high simulation runtimes.

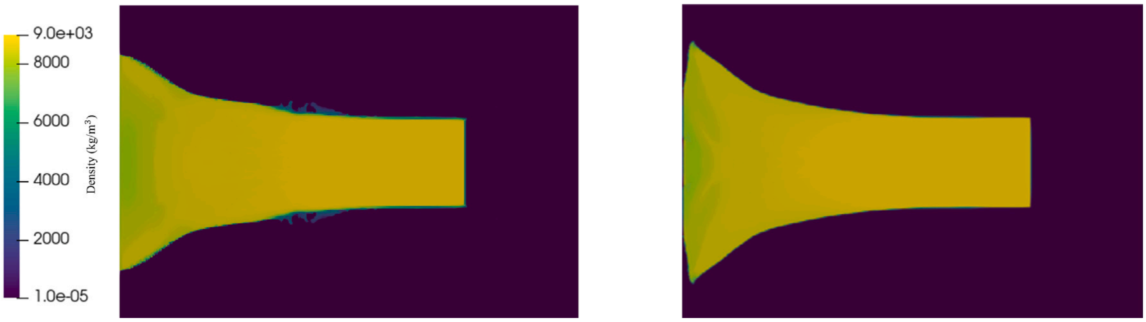

(a) B2 simulation with $f = 0.5$.

(b) B2 simulation with $f = 0.4$.

Fig. 12. A comparison of simulations frames at 20 μs with differing f.

AUTODYN. This analysis highlights the importance of incorporating artificial viscosity to mitigate shear wave instabilities and achieve a more accurate simulation of the Taylor rod deformation.

5.2. Cross code comparison

The deformation of a copper Taylor rod impacting a rigid boundary condition was simulated in AUTODYN and B2 at 100, 200 and 350 m/s. The test was performed at these velocities to evaluate the strength algorithm in B2 across a range of strain rates. The rod deformation in AUTODYN and B2 was analysed using both qualitative and quantitative criteria, including a visual comparison of the rod profiles and plots of the rod length and flared-end radius respectively (recall Fig. 9). The profile of the same rod deformation without the material strength algorithm (purely hydrodynamic) is also plotted, serving to highlight the effect of material strength on the deformation profile of the rod.

The Taylor rod at 100 m/s demonstrates a reasonable match between the codes. The plot comparing the length of the rod in Fig. 17 reveals the difference in the instantaneous rod length is minimal, increasing to just over 0.5% at 50 μs. The error in the flared-end radius is higher, rising to 14% at late times. Despite this difference, the plots of the profile demonstrate the simulations with the strength model are a significant improvement over the alternative without strength, particularly regarding the predicted flared-end radius. Further, the rod profiles depicted in Fig. 18 show the radius at the flared-end only diverges at late times. Indeed, the rod profile at 40 μs (Fig. 18(b)) reveals the simulation in B2 also successfully captured the location and magnitude of the barrelling in the rod adjacent to the flared-end. This suggests B2 largely captures the same behaviour as AUTODYN.

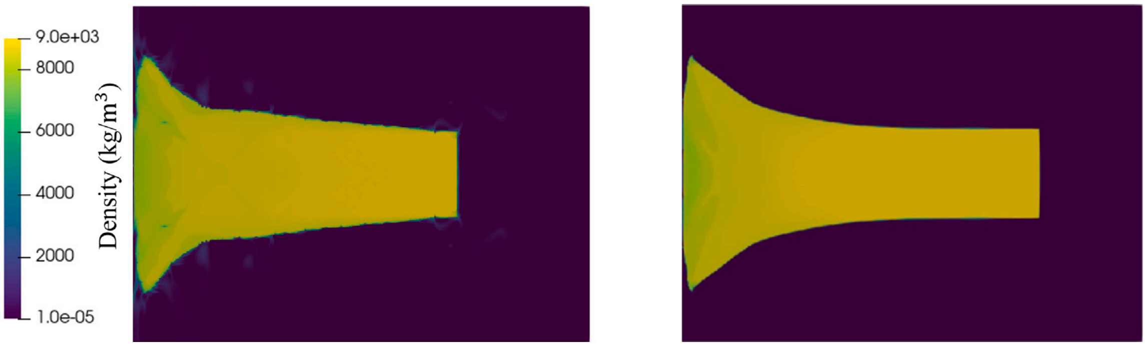

(a) B2 simulation frame 20 µs without the IG.

(b) B2 simulation frame 20 µs with the IG.

Fig. 13. Comparison between simulations without and with the IG. Non-physical blurring at the rod-vacuum interface visible in Fig. 13(a) are shown to have been eliminated in Fig. 13(a).

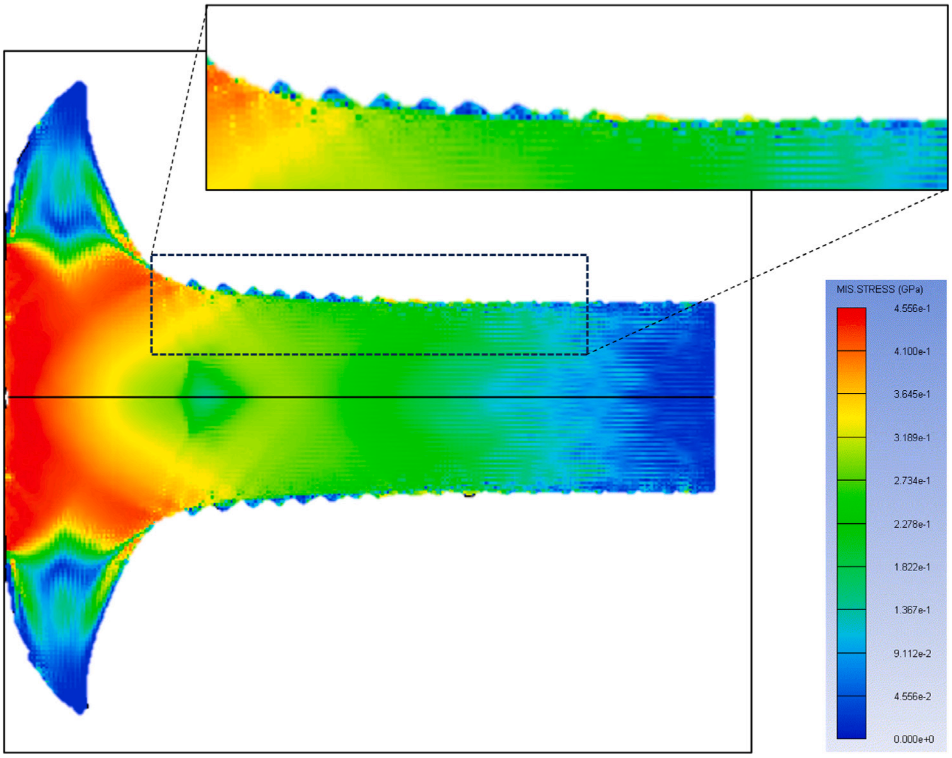

Fig. 14. Eulerian simulation of Taylor rod in AUTODYN. The frame shows serrated edge forms at the rod-vacuum interface.

(a) 10 µs

(b) 30 µs

(c) 50 µs

Fig. 15. Progression of the B2 simulation of the rod without the shear wave artificial viscosity modification.

The simulation of the Taylor rod at 200 m/s in B2 compares closely to its twin in AUTODYN. Overall, the deformed rod profile plotted over 80 µs in Fig. 20 appears visually similar: B2 successfully captured both the location and magnitude of both the barrelling in the region following the flared-end and the morphology of the flared-end itself. The most significant qualitative difference between the profiles predicted by B2 and AUTODYN is the deflection of the flared-end of the rod: the edges of the rod peel back to around 5 mm at late times

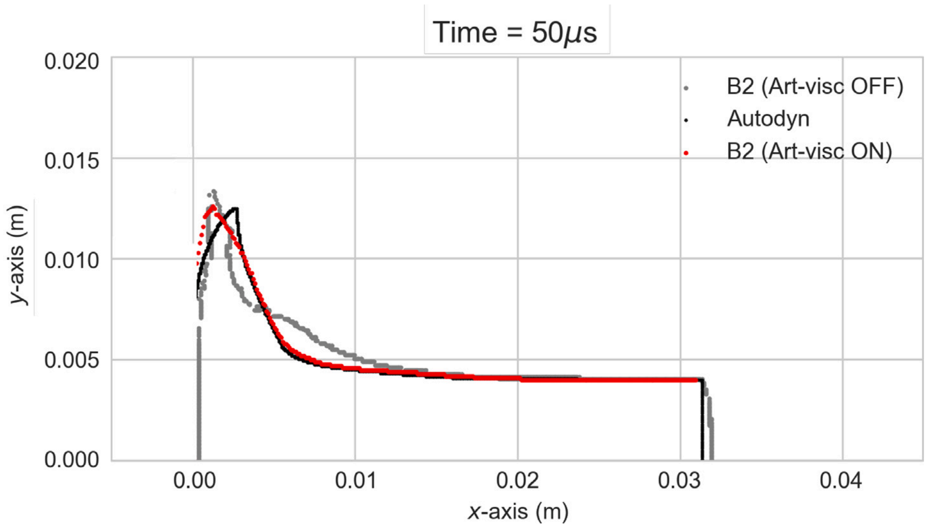

Fig. 16. Plot of the rod profile for a 200 m/s impact in B2, B2 without shear wave artificial viscosity and AUTODYN.

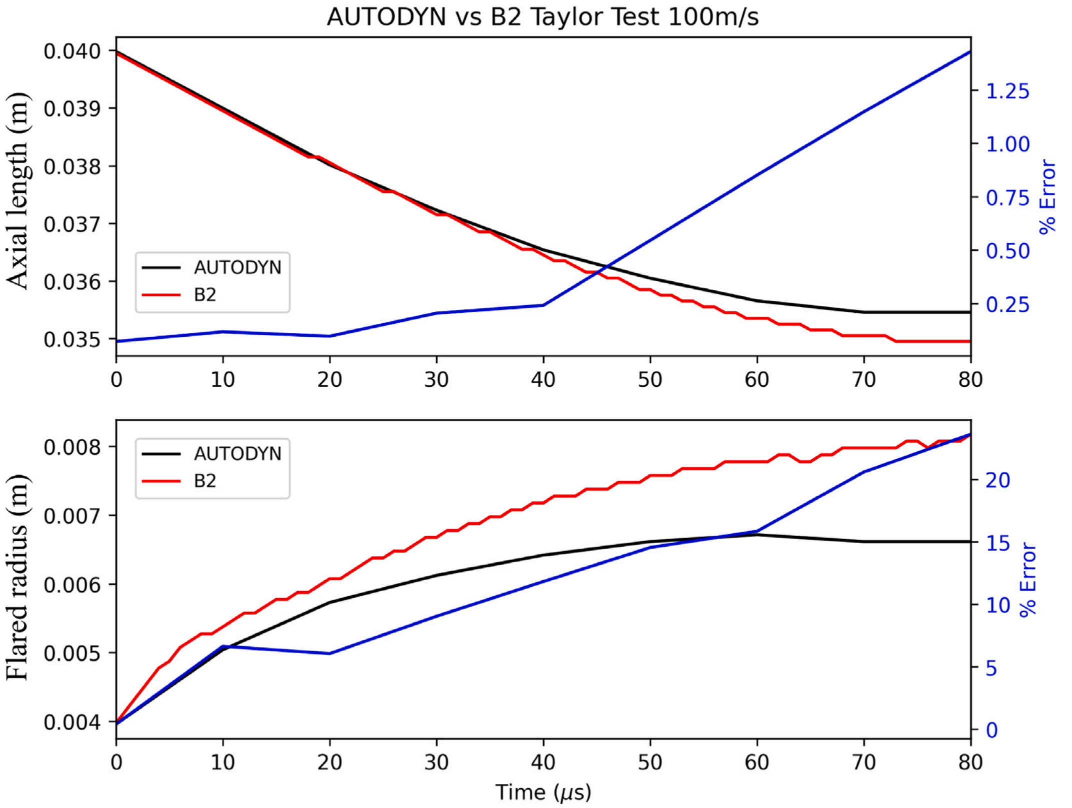

Fig. 17. Cross-code comparison showing plots of rod length, flared-end radius and the error between B2 and AUTODYN throughout the simulation of a 100 m/s Taylor anvil-on-rod test. The rod length in the simulations match closely, however, the error in the prediction of the flared-end radius rises to over 20% at late times.

in AUTODYN, but only to around 2.5 mm in B2. Despite this slight deviation in the profile at the flared-end, the plots in Fig. 19 show B2 closely matches the instantaneous crushed-end radius and rod length. The error in the axial length and radius remained below 1.5% and 5%, respectively, throughout the runtime.

Finally, while the simulation of the rod at 350 m/s was evaluated. The rods at 350 m/s have too high a velocity to display any distinctive barrelling behaviour, the plots in Fig. 22 demonstrate material strength remains important when predicting the rod length and flared-end radius. Fig. 22(c) shows the radius of the flared-end of the rod in B2 with strength off is far greater than B2 with strength or AUTODYN. As with the rod impact at 200 m/s, the flared-end of the rod in B2 does not peel back to the same degree as it does in AUTODYN. However, the plots in Fig. 21 show the overall error between the predicted length

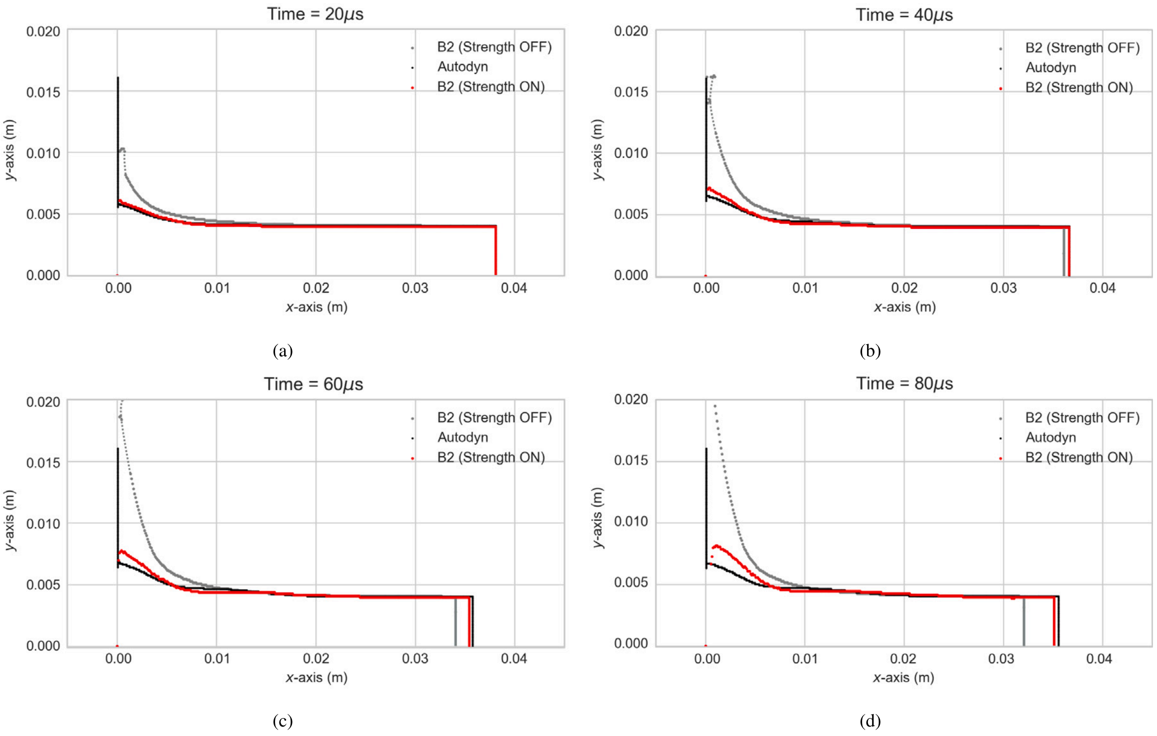

(a) (b)

(c) (d)

Fig. 18. Cross-code comparison of Taylor anvil-on-rod test simulations profiles at 100 m/s. B2 closely replicates the profile until 40 μs, after which time it overpredicted the flared-end radius.

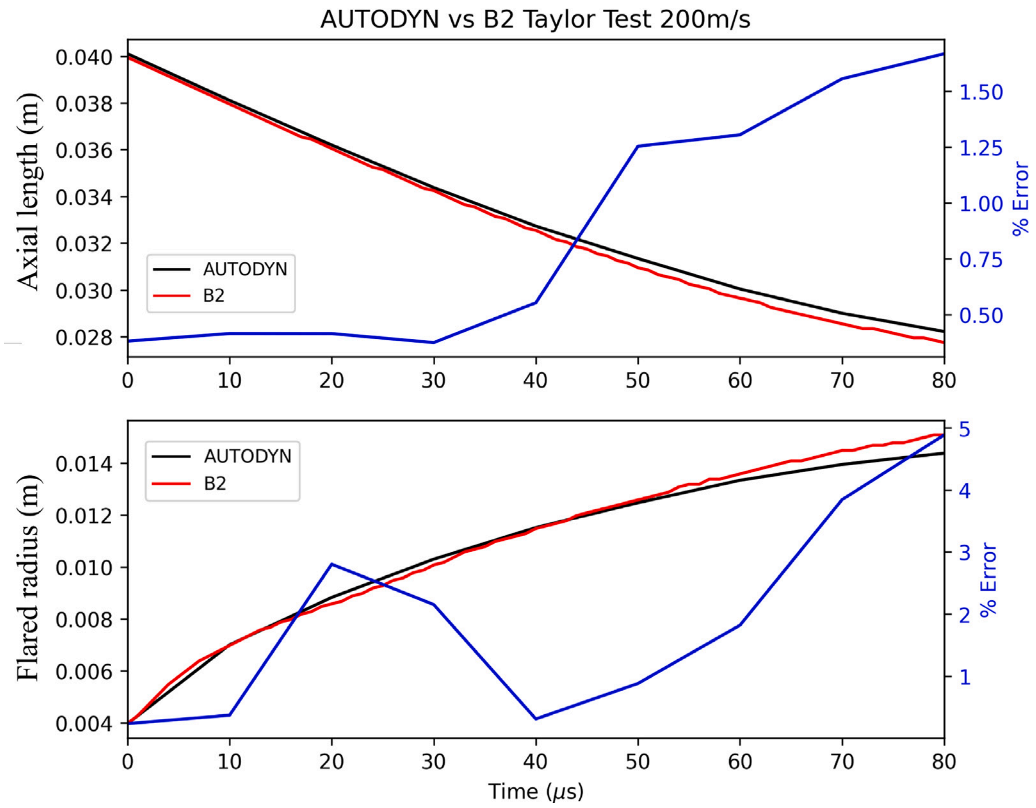

Fig. 19. Cross-code comparison showing plots of rod length, flared-end radius and the error between B2 and AUTODYN throughout the simulation of a 200 m/s Taylor anvil-on-rod test. The error between the axial length and flared-end radius in the codes remained below 1.5 % and 5 %.

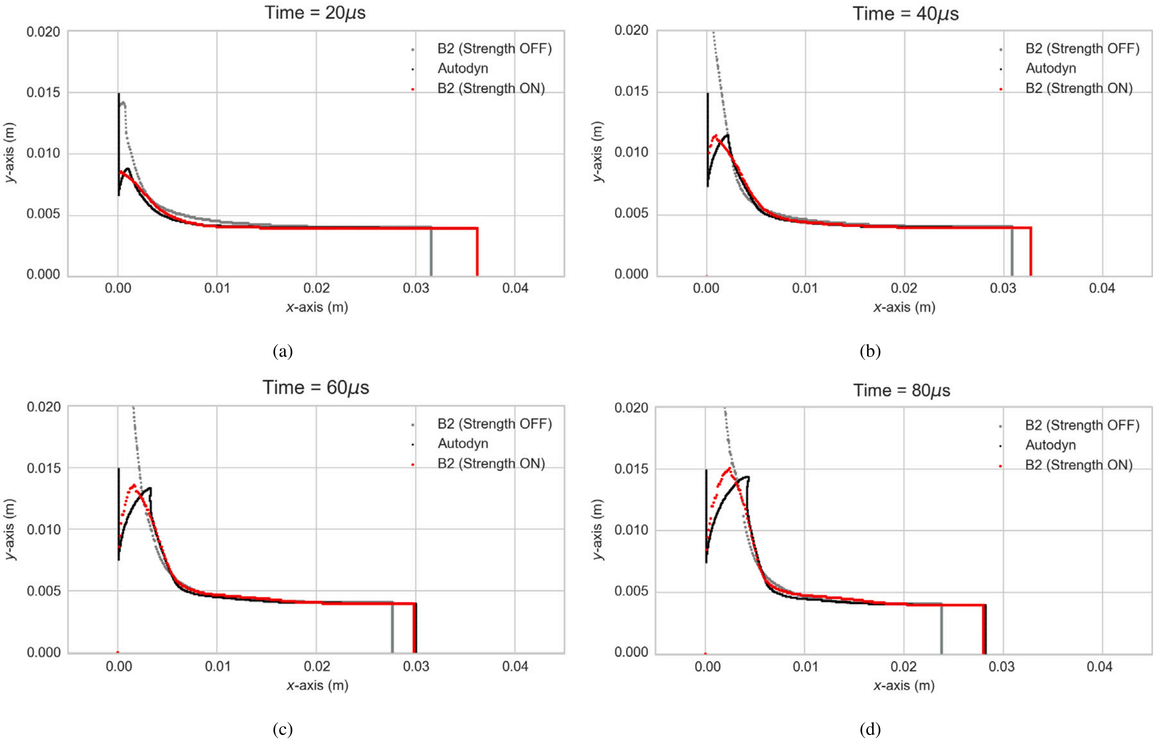

Fig. 20. Cross-code comparison of Taylor anvil-on-rod test simulations profiles at 200 m/s. B2 shows good qualitative agreements with AUTODYN, although the flared-end does not rebound as much.

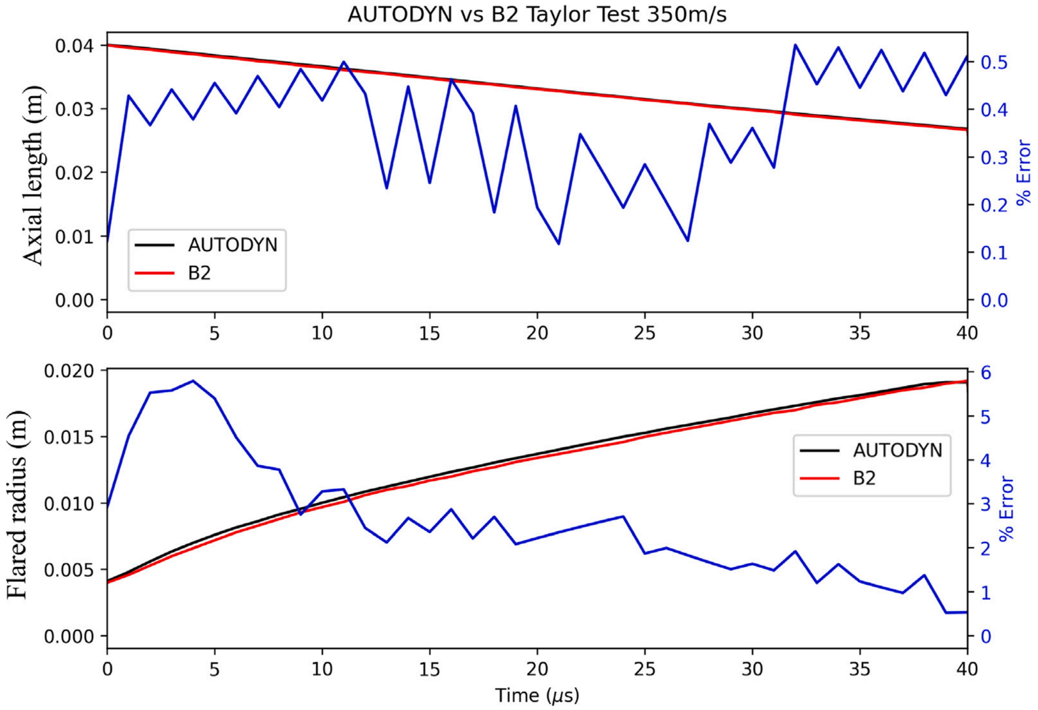

Fig. 21. Cross-code comparison showing plots of rod length, flared-end radius and the error between B2 and AUTODYN throughout the simulation of a 350 m/s Taylor anvil-on-rod test. The error between the codes at this velocity was the lowest out of the cases considered, where the axial length and flared-end radius maximum error was 0.5% and 6% respectively.

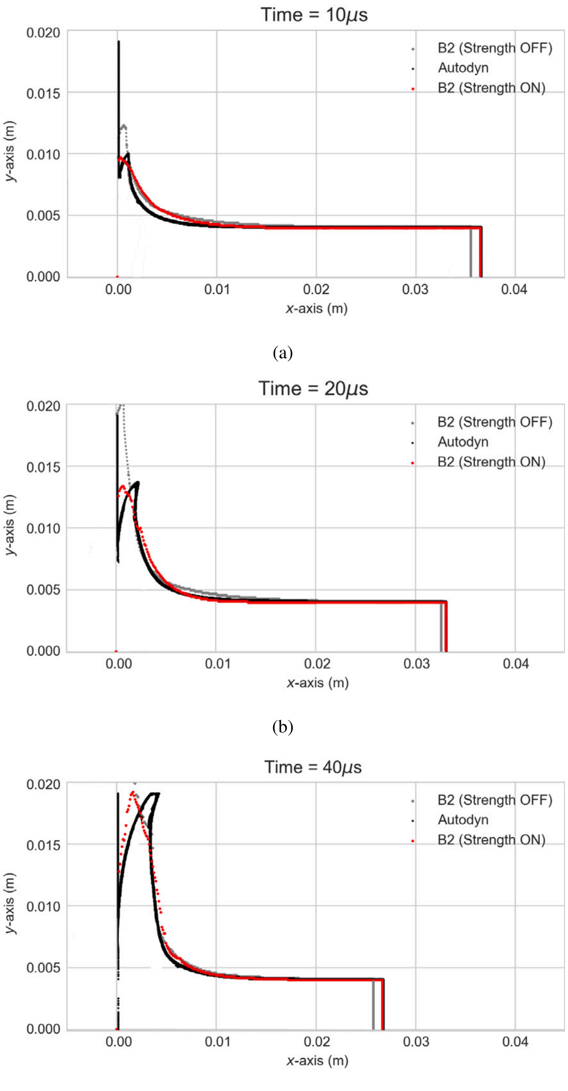

(a)

(b)

(c)

Fig. 22. Cross-code comparison of Taylor anvil-on-rod test simulations profiles at 350 m/s. The material strength model is clearly still important when predicting the flared-end radius, despite the high velocity of the impact.

and flared-end radius to be 0.5% and around 6% respectively. The error in the rod length prediction is the smallest of the three test cases and the magnitude and qualitative shape of the profile at the flared-end are similar.

6. Conclusions

In this work, the framework and implementation of a material strength model is demonstrated in a two-step Eulerian solution scheme in the hydrocode B2. This included the mathematical basis for the strength algorithm, which was incorporated into the first (Lagrangian) step. The results of Taylor test rod impact simulations in B2 were verified against those in AUTODYN. To replicate the AUTODYN rod deformation in B2 without requiring complex and costly interface reconstruction, several novel methods were developed. These methods are algorithmically simple, do not incur notable additional computational costs, and can be incorporated in their entirety into the solver's Lagrangian step, greatly simplifying their implementation, including:

- A complete method for calculation the stress tensor, force, and work components, including the locations in the cell where important variables such as the yield were stored. To the authors' knowledge, this information is not available elsewhere in open literature.
- The yield density dependence factor and adjustment to the stress tensor using the interface grid made it possible to remove unphysical diffusion and deformation due to shear forces generated between the high velocity rod and low velocity mixed-cells. This had the additional effect of greatly improving the runtime of simulations with strength enabled.
- The interface grid approach to implementing slip conditions at material boundaries enabled the algorithm to recognise separate material parts and maintain the accuracy of the rod interface at the anvil and vacuum in a manner that was both automatic and conducive to parallel processing.
- The additional component of artificial viscosity derived in this work successfully damped numerical instabilities introduced by shear forces, which when left unchecked resulted in a deeply unrealistic compressed Taylor rod profile.

The Taylor rod-anvil test served as a challenging scenario for evaluating the strength model in B2, as it exacerbated key issues commonly encountered when modelling solids in an Eulerian framework, such as simulating slip between materials and the deformation of a solid-vacuum interface over varying strain rates and long time periods. The successful reproduction of Taylor rod deformation results in B2 demonstrates that the implemented strength model is effective and can be applied to similar scenarios. In future work, B2 will be used to simulate high strain-rate behaviour in solids, including experiments that cannot be conducted using commercially available codes, such as the electromagnetic acceleration of flyers (Fitzgerald et al., 2024, 2025) and the collapse of cavities under strong shock loading.

CRediT authorship contribution statement

M.D. Fitzgerald: Writing – review & editing, Writing – original draft, Visualization, Validation, Methodology, Investigation, Formal analysis, Data curation, Conceptualization. **D.E. Eakins:** Writing – review & editing, Visualization, Validation, Supervision, Resources, Methodology, Investigation, Conceptualization. **N. Petrinic:** Supervision, Project administration. **E. Leggett:** Visualization, Software, Data curation. **N. Niasse:** Software, Investigation, Conceptualization. **J.D. Pecover:** Writing – review & editing, Validation, Supervision, Methodology, Investigation, Formal analysis, Conceptualization.

Declaration of competing interest

The authors declare that they have no known competing financial interests or personal relationships that could have appeared to influence the work reported in this paper.

Acknowledgements

The authors gratefully acknowledge the support provided by First Light Fusion

Data availability

Data will be made available on request.

References

Anderson, Jr., C.E., 1987. An overview of the theory of hydrocodes. Int. J. Impact Eng. 5 (1–4), 33–59.

Autodyn, A., 2005. Theory Manual Revision 4.3. Century Dynamics, Concord, CA.

Benson, D.J., 1992. Computational methods in Lagrangian and Eulerian hydrocodes. Comput. Methods Appl. Mech. Engrg. 99 (2–3), 235–394.

Benson, D.J., 1997. A mixture theory for contact in multi-material Eulerian formulations. Comput. Methods Appl. Mech. Engrg. 140 (1–2), 59–86.

Benson, D.J., 2002. Volume of fluid interface reconstruction methods for multi-material problems. Appl. Mech. Rev. 55 (2), 151–165.

Benson, D.J., Okazawa, S., 2004. Contact in a multi-material Eulerian finite element formulation. Comput. Methods Appl. Mech. Engrg. 193 (39–41), 4277–4298.

Burkett, M.W., 2019. Eulerian hydrocode modeling of a dynamic tensile extrusion experiment. In: Hypervelocity Impact Symposium, vol. 883556, American Society of Mechanical Engineers, V001T09A011.

Eakins, D., Thadhani, N., 2006. Instrumented Taylor anvil-on-rod impact tests for validating applicability of standard strength models to transient deformation states. J. Appl. Phys. 100 (7).

Faik, S., Tauschwitz, A., Iosilevskiy, I., 2018. The equation of state package FEOS for high energy density matter. Comput. Phys. Comm. 227, 117–125.

Fitzgerald, M., Pecover, J., Petrinic, N., Eakins, D., 2024. The effect of current rise time on the acceleration of thick flyers to hypervelocities using an electric gun. Int. J. Impact Eng. 184, 104814.

Fitzgerald, M., Pecover, J., Petrinic, N., Eakins, D., 2025. The design, modelling and testing of an electric gun load for the study of dynamic material properties. Int. J. Impact Eng. 198, 105179.

Johnson, G.R., Cook, W.H., 1985. Fracture characteristics of three metals subjected to various strains, strain rates, temperatures and pressures. Eng. Fract. Mech. 21 (1), 31–48.

Kemp, A., Meyer-ter Vehn, J., 1998. An equation of state code for hot dense matter, based on the QEOS description. Nucl. Instrum. Methods Phys. Res. Sect. A: Accel. Spectrometers Detect. Assoc. Equip. 415 (3), 674–676.

Lemke, R., Knudson, M., Hall, C., Haill, T., Desjarlais, P., Asay, J., Mehlhorn, T., 2003. Characterization of magnetically accelerated flyer plates. Phys. Plasmas 10 (4), 1092–1099.

McGlaun, J.M., Thompson, S., Elrick, M., 1990. CTH: A three-dimensional shock wave physics code. Int. J. Impact Eng. 10 (1–4), 351–360.

Pecover, J.D., 2015. Instability Growth for Magnetised Liner Inertial Fusion Seeded by Electro-Thermal, Electro-Choric and Material Strength Effects (Ph.D. thesis). Imperial College London, Available at https://spiral.imperial.ac.uk/handle/10044/1/26586.

Pecover, J., Chittenden, J., 2015. Instability growth for magnetized liner inertial fusion seeded by electro-thermal, electro-choric, and material strength effects. Phys. Plasmas 22 (10).

Taylor, G.I., 1948. The use of flat-ended projectiles for determining dynamic yield stress I. Theoretical considerations. Proc. R. Soc. Lond. Ser. A. Math. Phys. Sci. 194 (1038), 289–299.

Volkov, G., Borodin, E., Bratov, V., 2017. Numerical simulations of Taylor anvil-on-rod impact tests using classical and new approaches. Procedia Struct. Integr. 6, 330–335.

VonNeumann, J., Richtmyer, R.D., 1950. A method for the numerical calculation of hydrodynamic shocks. J. Appl. Phys. 21 (3), 232–237.

Walker, J.D., Anderson Jr., C.E., 1994. Multi-material velocities for mixed cells. In: AIP Conference Proceedings, vol. 309, (1), American Institute of Physics, pp. 1773–1776.

Westerling, L., 2002. An Implicit Method for a Strain Rate Dependent Constitutive Model Implemented in Autodyn as a User Subroutine. Tech. Rep. FOI-R–O3.

Youngs, D.L., 1982. Time-dependent multi-material flow with large fluid distortion. Numer. Methods Fluid Dyn.